Efficient Propulsion for
Versatile Unmanned Aerial Vehicles:
Studies in Mechanics and Control

A THESIS
SUBMITTED TO THE FACULTY OF THE GRADUATE SCHOOL
OF THE UNIVERSITY OF MINNESOTA
BY

Travis Henderson

IN PARTIAL FULFILLMENT OF THE REQUIREMENTS
FOR THE DEGREE OF
MASTER OF SCIENCE

NIKOLAOS PAPANIKOLOPOULOS

February, 2021

Acknowledgements

The successful completion of this work would not have been possible without the support of many, many people over the years that I have been thinking, researching, and writing. I have had countless models and mentors in the academic and research world, and most of them may not even realize that they have had such a profound impact on my knowledge base, work ethic and technical skill. I would like to thank all the past and present members of the solar UAV team at the Center for Distributed Robotics (CDR) for modeling such enthusiasm and willingness to work together to achieve something novel and exciting, no matter how tough the process might be; in particular, I would like to thank Scott Morton and Ruben D'Sa for bringing me onto the team as an inexperienced undergraduate and showing me the ropes. I would like to thank all the members of CDR for inspiring me to pursue high standards of excellence and novelty in whatever my hand finds to do. I could not have gotten to this point without the constant support, encouragement, and guidance of my advisor, Professor Nikos Papanikolopoulos, who through word and deed maintained belief in my work even when I was most doubtful of its value. This work would not have been possible without his tireless fight for support.

My family and friends have provided enormous love and support throughout the whole process of graduate school, for which I am profoundly grateful. To my mother and father and stepmother, thank you for providing support in so many ways: words of encouragement, wonderful food, clothes-both new and cleaned, transportation, and if these things weren't helpful enough, you always asked me about what I was learning and tried your best to understand the technical intricacies of this work and the excitement I have for it. To my brother and sister, I am so thankful for your empathetic excitement, encouragement, rides, food, and all the ways you have helped me to see the big-picture value and novelty in this work when I had gotten lost in the details. To my girlfriend,

who has graciously shown me patience that is not of this world, thank you for rejoicing with me in my successes, encouraging me in my failures, being patient with me in my long hours of isolated writing and research, fixing scrumptious food for next-day work lunches, and providing a kind and listening ear for many hours of half-explained technical content.

Time would fail me if I tried to adequately recognize my teachers, pastors, mentors, and friends over the years who nudged–or even pushed–me to seek higher excellence time after time. The current of their encouragement has helped to carry me through my engineering studies to this point.

Finally, I would like to thank and acknowledge my dependence on and trust in the God written about in the Christian Bible; the message of His loving, persevering commitment to Mankind is my ultimate inspiration.

Dedication

To friends who have encour'ged me so
To family who helps me grow
To Jesus Christ who lets me know
the Master Engineer;

Each earthly work yet to unfold
will someday hence be worn and old.
May this one help us all behold
the Master Engineer.

Abstract

This thesis presents a control algorithm for significantly enhancing the available thrust and minimizing the required electrical power consumption of a Variable-Pitch Propulsion (VPP) system, where the VPP system is made up of a brushless DC motor and a variable-collective-pitch propeller with its own servo motor. The variable-collective-pitch propeller mechanism has received recent attention because of the mechanism's capability to enhance thrust response bandwidth and propulsive efficiency compared to conventional Unmanned Aerial Vehicle (UAV) propulsion systems with rigid-geometry propellers; the mechanism has this capability due to a second mechanical degree of freedom in the propeller geometry, allowing the collective pitch angle of the propeller blades to vary according to actuation from a servo motor. When paired with a properly designed control algorithm, the motor speed and pitch angle can be tuned in real time to track prescribed thrust trajectories while satisfying some optimality condition.

Motivation for research into highly efficient VPP propulsion systems is encouraged by the intense interest from private and public sectors in UAVs that are capable of Vertical TakeOff and Landing (VTOL); while generally capable of both fixed-wing and hovering flight, VTOL UAVs with rigid-geometry propellers often exhibit short flight time due to non-optimal propulsion system efficiency across-the-board. Prior research into power-minimizing control strategies for small VPP systems has been targeted at multi-rotor platforms and has thus made assumptions that limit variation in the speed of propeller inflow and in the magnitude of thrust, thus limiting the technology's applicability to VTOL platforms. The control algorithm presented in this thesis is designed to accommodate for the wide range of air inflow speeds and thrust magnitudes through the following algorithm components: a linear feedback thrust controller with a nonlinear, adaptive feedforward thrust model derived from Blade Element Momentum propeller theory; an estimator to tune the thrust feedforward model parameters in real-time; and an Extremum Seeking algorithm for tracking the minimum-power control input configuration. Analysis of controller performance is discussed with reference to simulated and physical validation experiments.

Contents

List of Tables

List of Figures

Chapter 1

Introduction

The field of aerial robotics is constantly changing, and new models of Unmanned Aerial Vehicles (UAV) are being designed to accomplish tasks of increasing difficulty. UAVs have been found to be exceptionally useful for observing areas that are very large [2][3][4], observing sites which are distributed across large areas [5][6][7], or for providing sensing in areas where safety is a high priority [8]. In designing UAVs to meet these tasks, vehicles with Vertical Take-off and Landing (VTOL) ability have become highly desirable as they possess a high degree of maneuverability. However, one of the main obstacles to creating a small VTOL UAV with long endurance is that conventional propulsion systems are limited in the range of thrust and airspeed ranges for which they exhibit high performance. Often, a propulsion system that can facilitate VTOL maneuvers is inefficient during forward flight. This heuristic is graphically seen in Figure 1.1 which shows wind tunnel performance data of an APC propeller with a 10 inch radius and a nominal blade pitch of 4.7 inches per rotation [9]; The near vertical blue line shows a family of flight states characteristic of hover while the near-horizontal orange curve shows a family of flight states corresponding to level, fixed-wing flight. The propeller performance data show that the propeller does not perform efficiently in either state, and, even if it was designed for efficiency in one of the states, it would not be efficient in the other because of how separate the flight states are. This tradeoff which occurs during the propulsion system design process is an issue for all fixed-geometry propellers.

The Variable-Pitch Propulsion (VPP) system has been of interest to aviators for circumventing this flight envelope limitation for almost as long as modern flight has

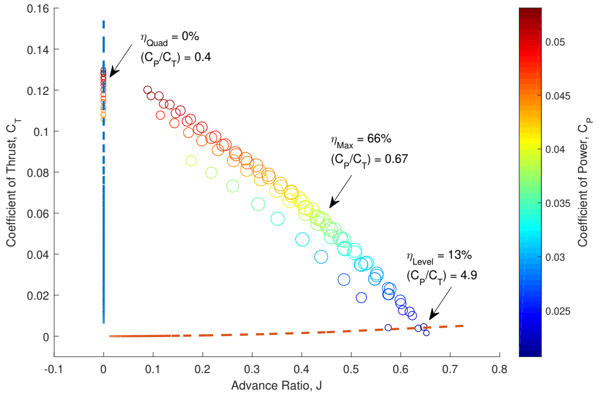

Figure 1.1: Dimensionless plot of performance data of APC 10x4.7SF propeller. Aerodynamic efficiency η is represented by the size of the data point, where a large point denotes high efficiency. The data points which are down and to the left of the main trend were taken at a lower propeller speed of about 4000 rpm, and thus exhibit reduced performance due to Reynolds number effects [1].

existed [10]. First used in the early 20th century to allow internal combustion engines on airplanes to operate near the optimal engine speed both during takeoff (i.e. at low air speed) and airborne flight (i.e. at high air speed), VPP saw perhaps its most advanced form when applied to helicopters. However, the more recent miniaturization of variable-pitch mechanisms has encouraged recreational remote pilots and researchers to experiment with variable pitch on UAVs.

Researchers have continued to explore the capabilities of the over-actuated VPP system. Interestingly, one of the first uses of variable pitch mechanisms on a small UAV was to increase the feasibility of a tail-sitter aircraft to achieve stable flight in fixed-wing and hovering configurations [11]. Showing that variable pitch increases aircraft agility prompted its application to multi-rotor platforms, enabling unprecedented improvements in aerobatic performance [12] and operation in multiple environments [13]. Others have used the VPP mechanism as a tool to partially decouple propeller thrust from propeller speed, thereby allowing propeller speeds to remain constant in the face of attitude disturbances, and even allowing all propellers on a multi-rotor to be driven by the same mechanical power source [14][15]. The introduction of these systems to research and industry contexts will facilitate the development of very capable UAVs

Figure 1.2: Examples of VTOL aircraft include (Top Left) American Robotics' self-managed UAV system for precision agriculture, (Top Right) Lynx VTOL UAV from Swift Radioplanes, LLC, (Bottom Right) a utility inspection platform from ULC Robotics Inc., and (Bottom Left) the KapetAir VTOL UAV.

applicable to precision agriculture, search and rescue, environmental monitoring and remote sensing tasks. Greater efficiency and performance in these tasks will be achieved through the proposed framework in this work.

Within approximately the last 10 years, a body of work associated with VPP has emerged which shifts the focus away from enhancing agility and toward increasing aircraft endurance. Some of the first mentions of the utility of VPP for tuning propulsion efficiency are found in [16] and [17], with the latter proposing a Kalman Filter-based extremum-seeking approach for arriving at a minimum-power control state. The authors in [18] and [19] proposed minimum-power-consumption controllers for multi-rotor UAVs. However, to the best of the authors' knowledge, no model of thrust as a function of motor speed, pitch angle and air speed has been developed for variable pitch systems with application to small UAVs. Avoiding the assumption of negligible air speed is crucial for designing a controller that is valid across a multi-mode UAV's full flight envelope.

This thesis builds on previous work which characterized VPP mechanisms in [20][21][22] by presenting an adaptive control framework which is made to function across a system's whole flight envelope. Key components of the control framework's development have been presented in [23] and [24]. While Chapter 2 describes the mathematical derivation of an adaptable thrust model, an estimation and control framework is presented in Chapter 3 and supported by validation results in Chapter 4. Concluding thoughts and descriptions of prudent future research directions are given in Chapter 5.

Chapter 2

System Modeling

2.1 System Modeling

The focus of this paper is on an individual Variable-Pitch Propulsion (VPP) system which may make up the whole or the part of a UAV of any type. However, since propulsion systems and UAVs have dynamics which are unequivocally coupled, a one-dimensional VPP-centric model of the propulsion-UAV coupling will be used for the remainder of this work as in Equation (2.1).

$$\dot{V} = -C_d V \left|V\right| - gsin(\gamma) + \frac{T}{m_{af}}. \tag{2.1}$$

Here, C_d is the bulk drag coefficient of the UAV-centric relative to the motion of that propulsion system; this is easiest to visualize on fixed-wing UAVs with a single propulsion system pointing in the direction of travel as in Figure 2.1, but for more complex geometries this quantity becomes more conceptual and would be something that would need to be learned from data. The constant g is the acceleration due to gravity, γ is the angle of the propulsion system's thrust vector relative to the horizon, T is the thrust produced by the propulsion system, and m_{af} is the airframe mass. V denotes the speed of air flowing past the propulsion system in a direction normal to the propeller disk area, and on a real aircraft this could be measured by a pitot tube. Vehicle airspeed at any time t is both defined by the vehicle's thrust-wise speed relative to ground and the wind's thrust-wise speed relative to ground as

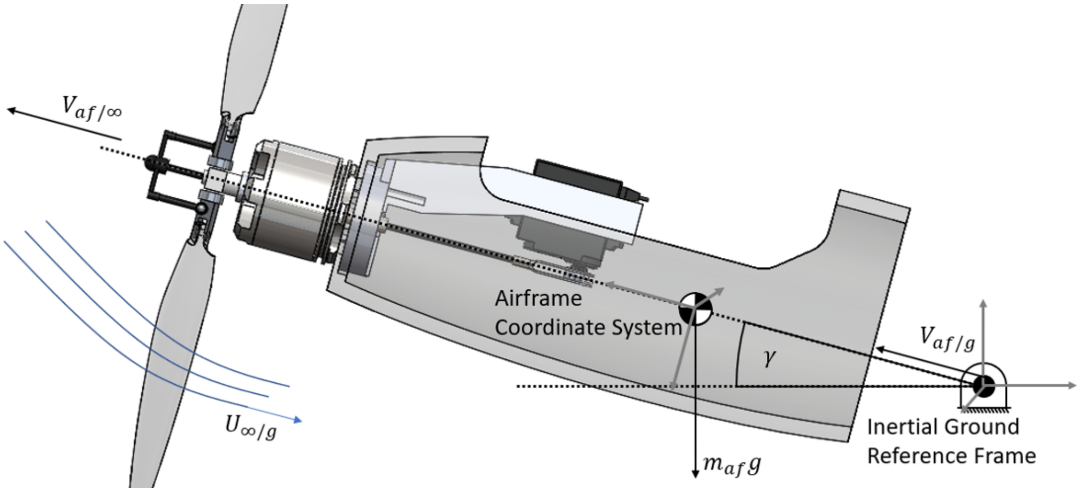

Figure 2.1: Example fuselage of an airframe on which the Variable-Pitch Propulsion system could be mounted.

$$V \equiv V_{af/\infty} = V_{af/g} - U_{\infty/g}. \tag{2.2}$$

Assuming that $U_{\infty/g}$ is constant or is changing about a constant value much slower than the UAV system dynamics means that $\dot{V} \approx \dot{V}_{af/g} = a_x$, where a_x is the inertial acceleration of the propulsion system in the thrust direction. As with air speed, this acceleration can be described by measurements commonly gathered on aerial systems with an inertial measurement unit by taking the measured longitudinal acceleration and subtracting out the contribution of gravitational acceleration due to the aircraft's attitude.

This section of the paper defines the components of the VPP system, the mathematical models associated with each system component, and presents some approximations of those models which will be used for control in the sections to follow.

2.1.1 System Topology

The VPP system of this work consists of a brushless DC motor, two propeller blades, a digital servo motor, and a mechanism connecting the blades to the servo horn. An example of an assembled VPP system is pictured below in Figure 2.2.

The output angle of a DC servo motor's horn can be acceptably modeled with the

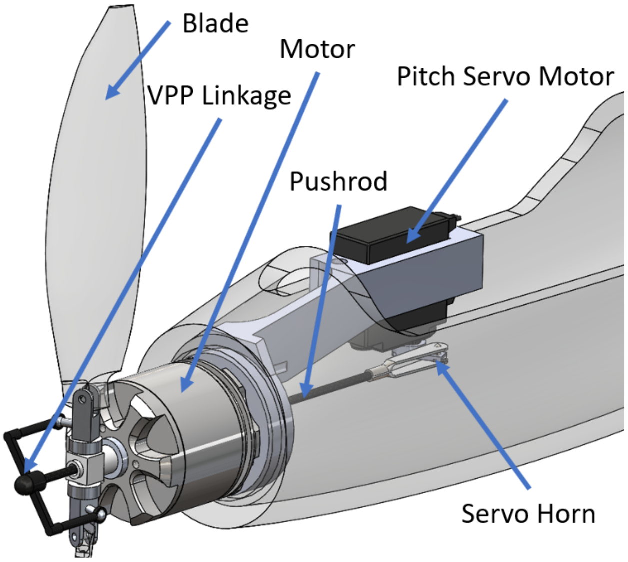

Figure 2.2: The VPP system studied in this work. In contrast with swashplate mechanisms, this mechanism for controlling pitch contains only the collective pitch actuation.

open loop transfer function

$$Z(s) = \frac{K_m}{s(T_m s + 1)} V(s) \tag{2.3}$$

where $Z(s)$ is the Laplace transform of the output servo angle $\zeta(t)$, K_m is an overall system gain from input voltage to output angle of the horn and T_m is an overall electro-mechanical time constant of the system. Assuming that $V(s)$ is defined by a PID controller on position error relative to a Laplace-transformed reference angle R_ζ, we can write

$$V(s) = (K_p + \frac{K_i}{s} + K_d s)(R_\zeta(s) - Z(z)). \tag{2.4}$$

We can then arrive at an expression for the so-called loop L:

$$L = PK = \frac{Z(s)}{E(s)} = \frac{K_m}{s(T_m s + 1)}(K_p + \frac{K_i}{s} + K_d s). \tag{2.5}$$

The transfer function from the Laplace-transformed servo angle reference $R_\zeta(s)$ to servo angle output $Z(s)$ can be formulated as

$$\frac{Z(s)}{R_\zeta(s)} = \frac{L}{1+L} = \frac{\frac{K_m(K_p+\frac{K_i}{s}+K_d s)}{s(T_m s+1)}}{(1+\frac{K_m(K_p+\frac{K_i}{s}+K_d s)}{s(T_m s+1)})}. \tag{2.6}$$

The closed-loop transfer function can be rearranged as in Equation (2.7). The non-unity term in the denominator has relative degree of -1, meaning that it goes to zero as $s \to 0$ and behaves like $\frac{T_m}{K_m K_d} s$ as $s \to \infty$. If the control gains have been appropriately chosen by the manufacturer to avoid underdamping under normal conditions, the transfer function behaves essentially like a first-order lag with time constant τ_ζ.

$$H_\zeta(s) = \frac{Z(s)}{R_\zeta(s)} = \frac{1}{\frac{s(T_m s+1)}{K_m(K_p+\frac{K_i}{s}+K_d s)}+1} \approx \frac{1}{\tau_\zeta s+1}. \tag{2.7}$$

The brushless DC motor can be represented with a nonlinear differential equation in the rotor's angular position θ with the parameters dependent on the armature electrical resistance R, the electrical motor constant k_e, a no-load current constant i_0, and a non-constant dissipation parameter C whose variation with time is dependent on motor speed, blade pitch angle, and vehicle air speed.

$$\ddot{\theta} = \frac{R\left(\left(\frac{-k_e}{R}(k_e+K_p) - C\left|\dot{\theta}\right|\right)\dot{\theta} - k_e i_0 + \frac{k_e}{R}(\tilde{V}_a - K_i\theta)\right)}{JR + k_e K_d} \tag{2.8}$$

The armature voltage input signal $\tilde{V}_a$ can, for most off-the-shelf Electronic Speed Controllers (ESC) executing kinematic control objectives (e.g. speed control), be reliably assumed to be a PID input signal with gains $[K_p,\ K_i,\ K_d]$ and desired values for rotor position, velocity, and acceleration, which can be expressed as

$$\tilde{V}_a = [K_i\ K_p\ K_d][\theta_d\ \dot{\theta}_d\ \ddot{\theta}_d]^T. \tag{2.9}$$

Equations (2.8) and (2.9) form a nonlinear filter with locally first-order characteristics relative to $\dot{\theta}$. Following the pattern of Equation 2.7, dynamics for the brushless DC motor can be approximated as

$$H_\omega(s) = \frac{\Omega(s)}{R_\omega(s)} \approx \frac{1}{\tau_\omega s+1}. \tag{2.10}$$

Because the control loops mentioned in these equations are often provided and tuned by manufacturers of servo motors and ESCs, the actuator dynamics of the servo motor and brushless DC motor will be approximated in the remainder of the paper by first-order response models with time constants τ_ζ and τ_ω, respectively.

2.1.2 Blade Element Theory

The flow of fluid around a propeller governs the thrust and drag characteristics. Blade Element Theory (BET) has been used successfully to model the thrust and drag characteristics of a propeller by modeling tangential and axial air flow as a function of the two-dimensional propeller geometry at a given radial distance r from the hub. Integrating these independent, two-dimensional flow field solutions along the blade length produces an estimate of thrust and shaft torque.

While BET has significant computational advantage over computing a 3D flow field using Finite Element Methods it still lacks usability in certain practical applications because it requires (1) an iterative solving method such as Newton-Raphson and (2) knowledge of propeller geometry including local pitch angle $\beta(r)$, local chord angle $c(r)$, and the local lift and drag behavior as a function of local blade Angle of Attack α (AoA). Some formulations of BET such as [25] specifically try to avoid direct knowledge of local airfoil performance by using parameterized formulations of local lift and drag which can be tuned with overall propeller performance data. As such, the differential thrust contribution is described by

$$\begin{aligned} dT =& \frac{\rho N_b}{2} U(r)^2 \big(C_L(\alpha(r)) cos(\phi(r)) \\ & - C_D(\alpha(r)) sin(\phi(r)) \big) c(r) dr \\ U(r) =& \sqrt{(\omega r)^2 + (V + \nu(r,\omega,V))^2} \end{aligned} \tag{2.11}$$

where ρ is air density, N_b is the number of blades, $U(r)$ is the magnitude of the local air flow vector seen by the propeller at radius r, C_L and C_D are the lift and drag coefficients which depend on the local Angle of Attack (AoA) $\alpha(r)$, $\phi(r)$ is the local angle between the plane of propeller rotation and $U(r)$, and $c(r)$ is the local chord length. The definition of $U(r)$ includes the local induced axial velocity $\nu(r,\omega,V)$, a quantity that can be solved for by comparing BET thrust predictions with BEMT predictions at each radius r. The following section will look at making a closed-form approximation of the thrust equation that can be learned from data.

2.1.3 Model Approximations

By substituting in the definition of $U(r)$ as well as the trigonometric identities of $cos(\cdot)$ and $sin(\cdot)$ written in terms of $U(r)$ and its axial or tangential component, we arrive at

$$\begin{aligned} dT =& \frac{\rho N_b}{2}\sqrt{(\omega r)^2 + (V+\nu(r,\omega,V))^2}\big(C_L(\alpha(r))\omega r \\ &- C_D(\alpha(r))(V+\nu(r,\omega,V))\big)c(r)dr. \end{aligned} \tag{2.12}$$

Using the simplified definitions of $C_L(\alpha)$ and $C_D(\alpha)$ provided in [25], we can employ the trigonometric identities $sin(2\cdot) = 2sin(\cdot)cos(\cdot)$ and $sin^2(\cdot) = \frac{1}{2}(1 - cos(2\cdot))$, as well as an order of magnitude approximation of $U(r)^{-\frac{1}{4}}$ to obtain Equations (2.13) and (2.14).

$$C_L(\alpha) = \frac{c_{l1}}{2}sin(2\alpha) \tag{2.13}$$

$$C_D(\alpha) = \left(c_{d0} + \frac{c_{d1}}{2} + 0.1\frac{c_{d2}}{\sqrt{\frac{\rho c(r)}{\mu}}}\right) - \frac{c_{d1}}{2}cos(2\alpha). \tag{2.14}$$

Putting these definitions into Equation (2.12) along with the approximation $\sqrt{(\omega r)^2 + (V+\nu(r,\omega,V))^2} \approx \omega r$ yields

$$\begin{aligned} dT \approx\ & M_1\Bigg(M_2 sin(2\alpha)(\omega r)^2 \\ & - (M_3(r) - M_4 cos(2\alpha))\omega r(V+\nu(r,\omega,V))\Bigg)c(r)dr \\ M_1 =\ & \frac{\rho N_b}{2},\ M_2 = \frac{c_{l1}}{2},\ M_4 = \frac{c_{d1}}{2} \\ M_3(r) =\ & \left(c_{d0} + \frac{c_{d1}}{2} + 0.1\frac{c_{d2}}{\sqrt{\frac{\rho c(r)}{\mu}}}\right). \end{aligned} \tag{2.15}$$

To provide transparency in derivation, the equation for a differential thrust contribution is partitioned into summed terms and written as follows:

$$\begin{aligned}
dT &\approx \sum_{i=1}^{5} dT_i \\
dT_1 &= N_1 r^2 c(r)\omega^2 sin(2\alpha)dr \\
dT_2 &= N_2(r)c(r)rV\omega dr \\
dT_3 &= N_2(r)c(r)r\nu(r,\omega,V)\omega dr \\
dT_4 &= N_3 c(r)rV\omega cos(2\alpha)dr \\
dT_5 &= N_3 c(r)r\nu(r,\omega,V)\omega cos(2\alpha)dr \\
N_1 &= M_1M_2,\ N_2(r) = -M_1M_3(r),\ N_3 = M_1M_4.
\end{aligned} \tag{2.16}$$

The local AoA $\alpha(r)$ is defined by the angle of incoming air flow $\phi(r)$, the local pitch angle of the propeller geometry $\theta(r)$, and the collective pitch angle θ_0. It turns out that, for 4-bar linkages with a long coupler link and input and output links of lengths similar to one another, θ_0 can be well approximated as a linear function of the servo horn angle ζ, which is useful because the mapping between ζ and θ_0 is nonlinear and often unknown or corrupted by process noise due to mechanism backlash. Therefore, the AoA is defined as

$$\begin{aligned}
\alpha(r) &= \theta_0 + \theta(r) - \phi(r,\omega,V) \\
&\approx (m\zeta + b) + \theta(r) - \phi(r,\omega,V).
\end{aligned} \tag{2.17}$$

The servo horn angle term can be broken out of the definition of α to give

$$\begin{aligned}
sin(2\alpha) &= sin(2m\zeta)cos(2(b+\theta(r)-\phi(r,\omega,V))) \\
&\quad + cos(2m\zeta)sin(2(b+\theta(r)-\phi(r,\omega,V))) \\
cos(2\alpha) &= cos(2m\zeta)cos(2(b+\theta(r)-\phi(r,\omega,V))) \\
&\quad - sin(2m\zeta)sin(2(b+\theta(r)-\phi(r,\omega,V))).
\end{aligned} \tag{2.18}$$

Plugging these definitions into Equation (2.16) and grouping terms which are functions of the integration variable r yields

$$\begin{aligned}
dT_1 &= N_1\omega^2 sin(2m\zeta)I_{1,1}(r,\omega,V) + cos(2m\zeta)I_{1,2}(r,\omega,V)\\
dT_2 &= V\omega I_2(r)\\
dT_3 &= \omega I_3(r)\\
dT_4 &= N_3 V\omega\Big(cos(2m\zeta)I_{4,1}(r,\omega,V) - sin(2m\zeta)I_{4,2}(r,\omega,V)\Big)\\
dT_5 &= N_3\omega\Big(cos(2m\zeta)I_{5,1}(r,\omega,V) - sin(2m\zeta)I_{5,2}(r,\omega,V)\Big).
\end{aligned} \tag{2.19}$$

The terms I_i are indisputably dependent on motor speed and air speed, but since the effect of their dependency is not easily computed without knowledge of the propeller geometry and additional computational expense, they will be treated as unknown parameters to be learned on-the-fly.

To release the parameter m from the sinusoid argument, a taylor approximation is made where $sin(2m\zeta) \approx 2m\zeta$ and $cos(2m\zeta) \approx 1 - 2m^2\zeta^2$. While this formulation does limit the applicability of the equation to large servo angles, it does enable m to be lumped with the rest of the unknowns. Therefore, Equation (2.16) can be rewritten as

$$\begin{aligned}
dT(r) \approx{} & (a_1(r)\zeta^2 + a_2(r)\zeta + a_3(r))\omega^2 + (a_4(r)\zeta^2 + a_5(r)\zeta + a_6(r))V\omega\\
& + (a_7(r)\zeta^2 + a_8(r)\zeta + a_9(r))\omega.
\end{aligned} \tag{2.20}$$

Upon integration of dT relative to r, each of the coefficients are transformed into new, unknown parameters b_i while ζ, ω and V are constant with respect to the integration. We then arrive at an approximate expression for thrust as a function of motor speed, air speed, and servo horn angle:

$$\begin{aligned}
T(\omega,\zeta,V,\mathbf{b}) \approx{} & (b_1\zeta^2 + b_2\zeta + b_3)\omega^2\\
+{} & (b_4\zeta^2 + b_5\zeta + b_6)V\omega\\
+{} & (b_7\zeta^2 + b_8\zeta + b_9)\omega.
\end{aligned} \tag{2.21}$$

2.2 Summary

This chapter details the assumptions about the Variable-Pitch Propulsion System design as well as the type of platform to which it is affixed. The motor and pitch servo dynamics were approximated with first-order models with known or estimated time constants. The remainder of the chapter was devoted to deriving a description of propeller thrust from Blade Element Theory, resulting in a 9-term closed-form equation which is linear in the coefficients. This linearity will be exploited for the purpose of online estimation in the next chapter.

Chapter 3

Control Design

This chapter presents two related, but distinct algorithms for achieving power-minimum control of a VPP system. Section 3.1 describes the first method that was explored. The method is simple to implement and requires sensors that are easily integrated onto an aerial platform. However, the method lacks robustness to both exogenous and endogenous disturbances. The second method which is introduced in section 3.2 is a sophistication of the first method, employing a more rigorously studied power optimization method and an on-the-fly modeling of thrust characteristics to increase performance and robustness to disturbances.

3.1 Perturb and Observe Control

This section explores the objective of controlling the 2-DoF VPP system to track a relatively constant desired state while converging to a minimum-energy-cost solution of the tracking problem. A pitch control algorithm for minimizing electrical power consumption is paired with a companion motor speed control algorithm for enforcing performance constraints related to the tracking of system setpoints. A diagram of the overall interconnection is shown in Figure 3.1. Interactions between the two algorithms are explored, and guidelines for achieving stable performance are presented.

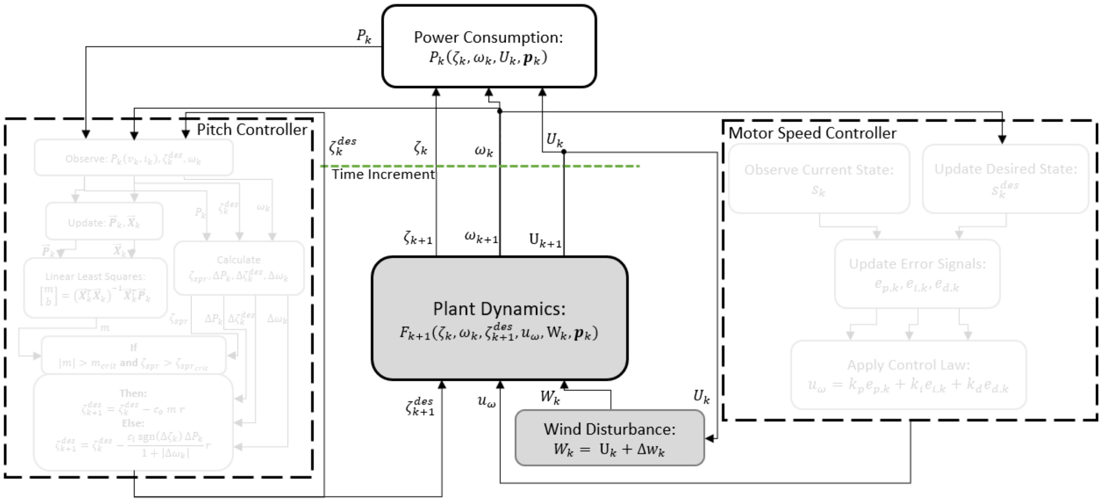

Figure 3.1: Flow chart of both algorithms interacting with the plant.

3.1.1 Pitch Control

The pitch control algorithm explored in this paper is based on the class of Power Point Tracking (PPT) algorithms, and in particular, it is closely based off of the Perturb and Observe (P&O) algorithm that is commonly used for harvesting maximum electrical power from solar arrays [26]. The algorithm itself can be applied to either maximization or minimization problems, and is used here to minimize expended electrical power. The main strength of P&O is that it does not require a dynamic model of the plant in order to track the optimum power point. However, because of this model-free design, P&O is also prone to diverging from the optimal point in periods of externally-induced transience. A flowchart of the pitch control algorithm is shown in Figure 3.2.

A simple P&O algorithm is used as the base of the pitch controller to locally explore the power-servo angle space for the perturbation direction of most reward at each point in time. Also at each point in time, the algorithm observes key quantities of power consumption, as well as the current desired servo angle ζ_k^{des} and motor speed ω_k. Note that the actual state ζ_k is not directly measured, but is assumed to be reached at each time step by ensuring that the execution time of the pitch control algorithm is much slower than the servo dynamics approximation given in equation 2.7. ζ_k^{des} and ω_k are added to a moving-average linear regression of power measurements $\vec{\mathbf{P}}_k$ with respect to

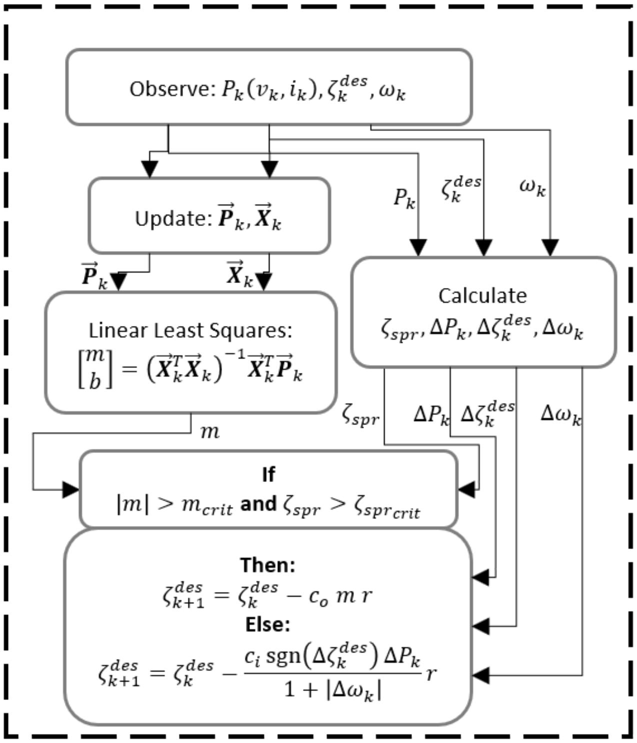

Figure 3.2: Flow chart of the composite Perturb and Observe algorithm used.

servo angles $\vec{\zeta}_k^{des}$ to create an approximation of the local gradient $\frac{\partial P}{\partial \zeta}$. The slope m of this gradient approximation is used to encourage a temporally smooth behavior in ζ. For situations where the gradient is relatively large, the next Perturbation step of the algorithm will be taken according to Equation (3.1)

$$\zeta_{k+1}^{des} = \zeta_k^{des} - c_o m r \tag{3.1}$$

where c_o is a user-defined proportionality constant and r is a characteristic stepsize of ζ^{des}.

This is done for two reasons. First, the moving average creates the notion of value history, a quality which often causes the quintessential form of P&O to diverge from the real solution. Additionally, as noted in [16], varying the pitch suddenly on a VPP system excites very fast dynamics, which would compromise the assumption of a quasi-steady state.

As ζ approaches an energy minimum, the slope m will go to zero. When this happens, the change in ζ_k^{des} also goes to zero if Equation (3.1) is still used. When either the absolute value of the slope of the estimated gradient falls below the threshold m_{crit} or the value ζ_{spr}, defined in Equation 3.2, falls below its associated threshold $\zeta_{spr_{crit}}$, the simple P&O perturbation is employed as in Equation (3.3) instead of the gradient descent-based method.

$$\zeta_{spr} = max(\vec{\zeta}_k^{des}) - min(\vec{\zeta}_k^{des}) \tag{3.2}$$

$$\zeta_{des} = \zeta_k - \frac{c_i sgn(\Delta\zeta_k)\Delta P_k}{1 + |\Delta\omega_k|} \tag{3.3}$$

Note that the P&O process assumes several things. First, it is a greedy algorithm, and in the absence of constraints on system performance, it will seek to minimize power consumption by reducing the aerodynamic load on the propeller. To avoid convergence to the trivial solution of a minimum-aerodynamic-load pitch angle, P&O requires a complementary controller to impose system performance constraints. Second, P&O assumes that no other factors are perturbing the power consumption in a significant way. This is a reasonable assumption for power point tracking on solar arrays, where change in available power due to irradiance fluctuations is several orders of magnitude slower than the tracking speed of the controller. In contrast, small-scale aerial robots often experience highly transient periods of power consumption. To help address the inevitability of relatively large state changes, the Perturbation rule in Equation (3.3) is scaled by the magnitude of motor speed change in the denominator. The idea behind this is to reduce the response of the pitch control algorithm to changes that are presumably caused by some other force to which the motor speed controller is reacting.

3.1.2 Motor Speed Control

Because the pitch algorithm has the role of minimizing cost without self-applying any constraints, a complementary algorithm for controlling the motor speed was developed in order to convert a kinematic or kinetic constraint into a power cost to which the pitch control can react. As shown in Figure 3.3, the motor speed controller's function is to track some desired reference signal, which in most cases may take the form of some aircraft state such as vehicle orientation or velocity. The reference signal is further assumed to be quasi-steady, that is, that any significant change in the setpoint is much slower than the response time of the motor speed controller. For the sake of simplicity, let any imposed constraint be a scalar quantity, represented by some quasi-steady state s_k in the state vector. A controller of almost any form could be applied within this framework, and in this case a PID controller was chosen.

The main feature of the motor speed controller is that, in order to impose constraints on the variable pitch minimization efforts, it must have a much faster response to changes in the plant dynamics than the pitch controller. If this condition is not met, the pitch controller will be able to circumvent the constraints and carry the system to an undesired part of the state-space.

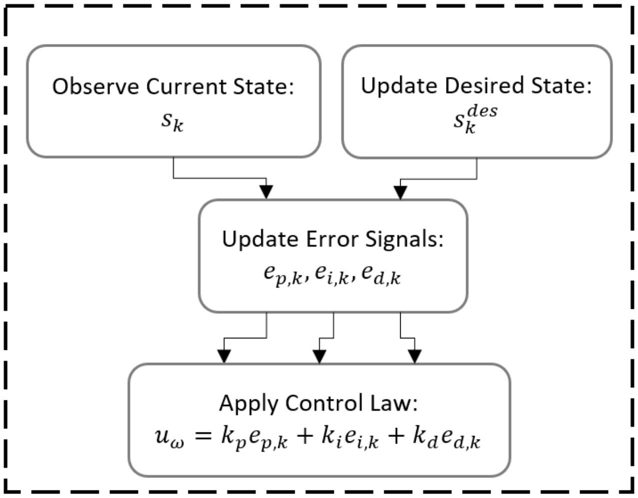

Figure 3.3: Flow chart of the motor speed control steps.

3.1.3 Limitations

Before moving on to the next section, it is important to highlight that the algorithm presented above does not address the cross-coupling between the pitch and motor controllers, and thus is vulnerable to destabilization in the face of disturbances from outside or inside the system or from oscillatory behavior due to mutual reactions between the pitch and motor controllers. Because of the simplicity of this control framework, stability is possible only if the thrust controller has a much faster response time than the pitch controller. Experiments in Chapter 4 will confirm this.

3.2 Extremum-Seeking Control

After validation experiments were conducted on the P&O control algorithm of Section 3.1, adjustments were made to help increase robustness and performance. Two main observations were seen: first, the Perturb and Observe approach to pitch control introduces high-frequency noise into the system and needs to be temporally smoothed in practice in order to avoid destabilizing the controller. This smoothing reduces the convergence rate of power minimization, an undesired consequence. Second, there is no model of how the power minimization process affects thrust tracking. Addressing these two ideas became the main focus of the following controller. Figure 3.4 presents the estimation and control framework; in the improved framework, a feedforward thrust model T_{ff} is employed to account for the innate coupling between servo angle and thrust. The Perturb and Observe algorithm is replaced by the related method of Extremum Seeking, denoted in the figure by ES, following the work of Krstic et al. [27][28]. Finally, an Extended Kalman Filter EKF estimates thrust measurements and uses these to tune the parameters of T_{ff}. The feedback controller $K(s)$ performs the same function as it did in the previous algorithm by taking an error signal defined by a reference and state information and providing a motor-speed signal to drive the system denoted by VPP toward a desired thrust.

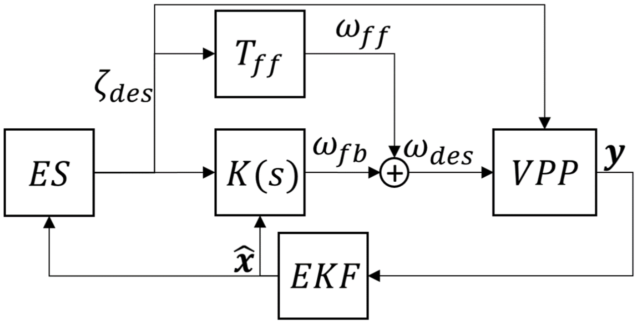

Figure 3.4: Diagram of the overall control framework.

3.2.1 Robust Thrust Control

The thrust model presented in this section draws from the Blade Element Theory simplified model of thrust developed in Section 2.1. In particular, the model expresses thrust's dependence on motor speed, air speed and servo horn angle, which provides a very useful feedforward motor speed ω_{ff} for creating a desired thrust T_{des}. This can be expressed as

$$\begin{aligned}\omega_{ff} &= -\frac{b_{ff}}{2a_{ff}} + \sqrt{\left(\frac{b_{ff}}{2a_{ff}}\right)^2 - \frac{c_{ff}}{a_{ff}}} \\ a_{ff} &= b_1\zeta^2 + b_2\zeta + b_3 \\ b_{ff} &= (b_4V + b_7)\zeta^2 + (b_5V + b_8)\zeta + (b_6V + b_9) \\ c_{ff} &= -T_{des}\end{aligned} \tag{3.4}$$

where w_{ff} is a feedforward signal which may be fed into the plant VPP in parallel with a PID feedback trim controller $K(s)$. In using the thrust model as a feedforward signal, precautions must be taken to ensure the mathematical and physical validity of the signal value. The choice of plus sign in front of the square root encourages a positive value of ω_{ff}. However, simply choosing a plus sign is not sufficient to guarantee a positive real feedforward signal. Table 3.1 shows all possible cases of signs of the thrust model coefficients, and all of the possible resulting signs of ω_{ff}. Although the first four cases are the most expected since these are the cases for which the desired thrust is positive, it can be seen that by manipulating ζ to enforce the condition

$$a_{ff}(\zeta, t) \cdot T_{des}(t) > 0 \tag{3.5}$$

at time t, the existence of a positive real value of ω_{ff} is guaranteed regardless of the coefficients' relative magnitudes. This makes intuitive sense because this constrains the thrust model's concavity to match the sign of the T_{des}.

In addition to guaranteeing a positive real value, one ought also to ensure that the feedforward motor speed is reachable (i.e., finite and within control saturation limits). Unreachable thrust in the context of a VPP system occurs when the particular servo angle at time t is too small to produce the thrust within the range of reachable motor speeds. For propeller blades with cambered airfoils, this condition becomes more likely to occur when the propeller blade pitch is at small or negative pitch angles. Under the current control structure proposed in Figure 3.4, this situation would drive the motor speed to its upper saturation limit. Assuming that the thrust model coefficients b_i have been estimated to adequate confidence in the neighborhood of the saturation limit,

Case	$\mathbf{a_{ff}}$	$\mathbf{b_{ff}}$	$\mathbf{c_{ff}}$	$\omega_{\mathbf{ff}}$
1	$-$	$-$	$-$	$-i$
2	$+$	$-$	$-$	$+$
3	$-$	$+$	$-$	$+i$
4	$+$	$+$	$-$	$+$
5	$-$	$-$	$+$	$+$
6	$+$	$-$	$+$	$-i$
7	$-$	$+$	$+$	$+$
8	$+$	$+$	$+$	$-i$

Table 3.1: Analysis of the possible signs of the feedforward thrust signal ω_{ff} given signs of thrust model coefficients. The addition of "i" in some of the sign label of ω_{ff} indicates the possibility of obtaining complex roots, depending on the sign of the discriminant.

thrust reachability can be maintained. The terms of Equation 2.21 can be grouped according to the order of the servo angle ζ, and by bringing the desired thrust to the right side of the equation and solving for the roots of ζ in the same manner as Equation 3.4, estimates of the thrust-critical servo angles ζ_{crit} are calculated as

$$\begin{aligned}
\zeta_{crit} &= -\frac{b_{crit}}{2a_{crit}} \pm \sqrt{\left(\frac{b_{crit}}{2a_{crit}}\right)^2 - \frac{c_{crit}}{a_{crit}}} \\
a_{crit} &= b_1\omega_{crit}^2 + b_4\omega_{crit}V + b_7\omega_{crit} \\
b_{crit} &= b_2\omega_{crit}^2 + b_5\omega_{crit}V + b_8\omega_{crit} \\
c_{crit} &= b_3\omega_{crit}^2 + b_6\omega_{crit}V + b_9\omega_{crit} - T_{des} \\
\omega_{crit} &= (1-\epsilon)\omega_{max},\ 0 < \epsilon < 1
\end{aligned} \tag{3.6}$$

where ϵ is a designer-chosen safety margin to prevent motor speed saturation. In practice, rules for the value of ϵ may be developed which parameterize ϵ as a function of thrust and perhaps other factors. For most cases it is safe to assume that the larger, more positive root ζ_{crit}^+ is the relevant root. Thus, thrust reachability is preserved to within an ϵ safety margin when

$$a_{crit}T_{des}(\zeta - \zeta_{crit}^+) \geq 0. \tag{3.7}$$

Because the VPP system is a multi-input nonlinear system, any set of PID gains which satisfies certain performance and stability conditions at a certain operating point may not satisfy those conditions at another point in the state space. The feedforward thrust model attempts to describe the nonlinearity, so some utility can cautiously be gained by linearizing the feedforward model and assuming it as an adequate approximation of local plant behavior given a set of well-estimated parameters b_i.

Given that the VPP actuators are modeled as first-order filters (see Section 2.1), we next focus on linearizing the feedforward thrust model about an operating speed ω_0. We can transform the motor speed and thrust signals to be centered on the origin as

$$\begin{aligned} \widetilde{\omega} &= \omega - \omega_0 \\ \widetilde{T} &= T - T_0 \\ \widetilde{T}_{ref} &= T_{ref} - T_0 \end{aligned} \tag{3.8}$$

where T_0 is the value of the thrust produced at the linearization point and T_{ref} is the reference thrust signal. Using a first-order Taylor series approximation to linearize the feedforward thrust model about ω_0 gives

$$T(V, \omega, \zeta) \approx T_0 + K_T \widetilde{\omega} \tag{3.9}$$

where K_T is the linear transfer function gain from motor speed to thrust defined as

$$K_T \equiv \left. \frac{\partial T(V, \omega, \zeta)}{\partial \omega} \right|_{V_0, \omega_0, \zeta_0} = 2a_{ff}\omega_0 + b_{ff} \tag{3.10}$$

Implicit in Equation 3.10 is the assumption that any time variation of the gain or phase delay in the motor speed-to-thrust transfer function is negligible. Although this is not truly the case with respect to fluid dynamics [29][30], it is often neglected in modeling small-scale aerial robots. However, a separate source of lag which must be accounted for arises from the physical method of controller implementation. The zero-order hold behavior that results from the most common implementations of a controller onto a discrete microcontroller unit can be modeled with a first-order Pade approximation as[31]

$$ZOH(s) \approx \frac{1}{0.5T_s s + 1} \tag{3.11}$$

.

where T_s is the update period of the controller. Lumping this in with the plant dynamics, we have

$$P_m(s) = K_T H_\omega(s) ZOH(s) = \frac{K_T}{(\tau_\omega s + 1)(0.5T_s s + 1)}. \tag{3.12}$$

Following the design rules of Skogestad and Postlethwaite [32], a PI controller $K(s)$ is written as

$$K(s) = \frac{\tau_{\omega 0}}{K_{T_0}\tau_c}\left(1 + \frac{1}{\tau_I s}\right) \tag{3.13}$$

where $\tau_{\omega 0}$ and K_{T_0} are assumed values for the motor time constant and linearized thrust gain, respectively, τ_c is a controller tuning parameter allowing for a compromise between stability and performance, and $\tau_I = min(\tau_{\omega 0},\ 4\tau_c)$.

$\tau_{\omega 0}$ and K_{T_0} may be chosen by ballpark estimation from performance data, but because these values will, in general, change during the course of operation, a robust stability analysis is employed. Table 3.2 gives the values used in the linear controller for robustness analysis and simulation along with the pitch controller. The value for K_{T0} was arrived at by assuming that a maximum normalized motor speed (i.e. $\omega = 1$) produces maximum normalized thrust while also naively assuming the conventional quadratic relation between thrust and motor speed $T = \mathcal{C}\omega^2$. This constraint implies that $\mathcal{C} = 1$ at this operating point and that K_T at this point is equal to 2.

Name	**Value**	**Units**
K_T	$2 \pm 50\%$	-
τ_ω	$3.2E-3 \pm 50\%$	s
T_s	0.02	s
τ_c	$1.0 \cdot T_s$	s
τ_I	$\tau_{\omega 0}$	s

Table 3.2: Values used for robust analysis and simulation of motor speed controller.

The reality is that the motor speed controller will need to be tuned before any thrust model parameters are estimated, so it is important that the motor speed controller be robust to comparatively large changes in the plant model parameters. Figure 3.5 summarizes the stability and performance characteristics for randomly sampled plants within the ±50% variation of K_T and τ_ω. The controller has a worst-case tracking error of $-14\ dB$ at a disturbance frequency of $\omega_d = 2\pi\ rad/s$. If the disturbance frequency is halved, tracking error is improved to nearly $-20\ dB$ at worst. These two frequencies mark the range of expected frequency activity produced by the pitch controller talked about in the next section.

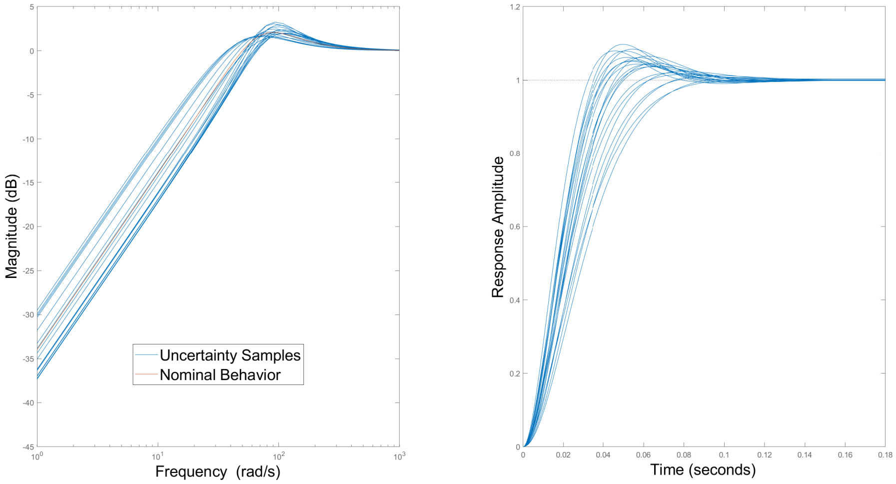

Figure 3.5: Graph of the closed loop Sensitivity of the motor speed subsystem (left) and a corresponding plot of the step responses (right) under 50% uncertainty in the linearized thrust gain K_T as well as in the first-order motor time constant τ_ω.

3.2.2 Stable Pitch Control

To improve upon the pitch controller presented in Section 3.1, the Extremum-Seeking (ES) control algorithm from [27] was used. This particular method, shown in Figure 3.6, superimposes a sinusoidal perturbation of frequency ω_p onto the estimated optimal servo angle $\hat{\zeta}_{des}$. This perturbation excites a response in the power consumption P of the VPP plant. The power output of the plant is then filtered to remove low-frequency bias, demodulated with the original perturbation, and then integrated to get the estimated optimal servo angle. Over time, the ES algorithm will drive $\hat{\zeta}_{des}$ to a minimum-power-consumption configuration given an approximately constant thrust and air speed. The advantage of this approach over the P&O approach is that the algorithm updates $\hat{\zeta}_{des}$ in a time-averaged manner due to the sinusoidal nature of the perturbation. Secondly, the perturbation frequency is chosen and is therefore known before run-time, making it easier to filter out changes in power that do not correspond to the input perturbation. For this implementation onto the VPP system, several extra elements were added to the system to improve performance. A low pass filter with cutoff frequency ω_{lp} was added according to the design recommendations of [33] after demodulation to further limit

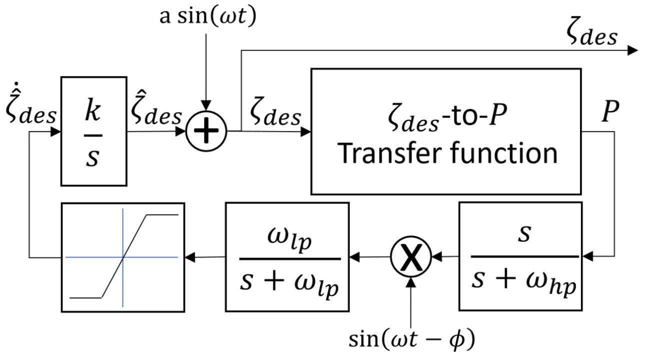

Figure 3.6: Convergence of the real thrust and thrust feedforward model to a constant reference at 0.5, 50% of nominal capacity.

high-frequency changes in $\hat{\zeta}_{des}$, and hard saturation limits were also added to clamp the magnitude of $\dot{\hat{\zeta}}_{des}$. The input perturbation $a\ sin(\omega t)$ was modified with a time-pause entrance and exit condition to prevent the perturbation from exciting the system undesirably during feedforward model learning or strong thrust transients.

3.2.3 Extended Kalman Filter

An Extended Kalman Filter (EKF) is employed to provide estimation of key propulsion states from noisy measurements and also to learn the coefficients of a nonlinear feedforward model of thrust, the form of which has been derived in Section 2.1. In some cases, a reduced order EKF can be used if there is sufficient confidence in measured states such that they can be used as measured.

The EKF used in this paper is a discrete time formulation with state $\mathbf{x} \in \mathbb{R}^n,\ n = 15$ and output $\mathbf{y} \in \mathbb{R}^m,\ m = 6$ modeled respectively by

$$\mathbf{x}_{k+1} = f(\mathbf{x}_k) + \mathbf{w}_k \tag{3.14}$$

$$\mathbf{y}_k = h(\mathbf{x}_k) + \mathbf{v}_k \tag{3.15}$$

where $\mathbf{x}_k = [V_k\ \omega_k\ \zeta_k\ P_k\ T_k\ a_{x,k}\ \mathbf{b}_k^T]^T$, $\mathbf{y}_k = [V_k\ \omega_k\ \zeta_k\ P_k\ T_k(V_k, a_{x,k})\ a_{x,k}]^T$, and $\mathbf{w}_k$ and $\mathbf{v}_k$ are zero-mean, Gaussian random variable vectors in $\mathbb{R}^n$ and $\mathbb{R}^m$ modeling the noise in the process and measurement models, respectively. Note that the measurement of thrust in $\mathbf{y}_k$ is created based on combining noisy measurements from airspeed V_k

and gravity-compensated longitudinal acceleration $a_{x,k}$ in Equation (2.1). The process model for the estimated VPP states not including the coefficients of the thrust model is written as

$$\mathbf{A}_a = \begin{bmatrix} (1 - \frac{\Delta t C_d}{m_{af}}|V_k|) & \mathbf{0}_{1x3} & \frac{\Delta t}{m_{af}} & 0 \\ 0 & \mathbf{I}_{3x3} & \mathbf{0}_{3x1} & \mathbf{0}_{3x1} \\ 0 & \mathbf{0}_{1x3} & 0 & 0 \\ 0 & \mathbf{0}_{1x3} & 0 & 1 \end{bmatrix}. \tag{3.16}$$

The process model $f(\mathbf{x}_k)$ is defined as

$$f(\mathbf{x}_k) = \begin{bmatrix} \mathbf{A}_a & \mathbf{0}_{6x9} \\ \mathbf{0}_{9x6} & \mathbf{I}_{9x9} \end{bmatrix} \mathbf{x}_k + \begin{bmatrix} \mathbf{0}_{4,1} \\ 1 \\ \mathbf{0}_{10x1} \end{bmatrix} T(\omega_k, \zeta_k, V_k, \mathbf{b}_k). \tag{3.17}$$

The measurement $h(\mathbf{x}_k)$ is written as

$$h(\mathbf{x}_k) = \begin{bmatrix} \mathbf{I}_{6x6} & \mathbf{0}_{6x9} \end{bmatrix} \mathbf{x}_k. \tag{3.18}$$

The variances of the process and measurement models are assumed to be matrices $\mathbf{Q} \in \mathbb{R}^n$ and $\mathbf{R} \in \mathbb{R}^m$, respectively initialized as

$$\begin{aligned} \mathbf{Q} &= diagonal\left(\begin{bmatrix} \mathbf{I}_{1x6} & \frac{1}{2}\mathbf{I}_{1x9} \end{bmatrix} \right), \\ \mathbf{R} &= diagonal\left(\begin{bmatrix} 2 & 1 & 1 & 1 & 3 & 2 \end{bmatrix} \right). \end{aligned} \tag{3.19}$$

3.3 Summary

This chapter details the design of two control algorithms. The first utilized only a PID feedback motor speed control algorithm and a modified Perturb and Observe (P&O) algorithm for power minimization. Although this partitioned-controller showed the utility of real-time control on a physical system, the algorithm design lacked robustness because it did not attempt to model the coupling between pitch angle and thrust; furthermore, the P&O algorithm promoted controller instability when subject to high-frequency disturbances. To address these shortcomings, the entire control algorithm was redesigned to execute thrust control with a nonlinear adaptive feedforward element in parallel with the feedback PI control law. The P&O approach to power minimization was replaced with a time-averaged Extremum-Seeking algorithm, and several filters and state logic conditions were added to define when the minimization process was allowed to operate.

Chapter 4

Experiments

4.1 P&O Control Experiments

To validate the controller framework described in Section 3.1, two categories of hardware-based experiments were conducted. The first experimental testbed was an enclosed, table-mounted lever arm created to test the stability and convergence characteristics of the controller framework in static-thrust conditions similar to a vertical flight. For the second experimental testbed, an E-flite Radian remote control glider was used to test the controller performance during a fixed-wing aerial flight.

4.1.1 Table-Mounted Testbed

A series of experiments were performed on the testbed in which the motor speed controller was allowed to bring the Lever Arm to a desired setpoint θ_{des}, usually 0° as is pictured in Figure 4.1. Upon reaching an approximately steady state, pitch control was activated and allowed to explore the state space for a minimum, subject to the need for maintaining an arm attitude close to θ_{des}.

The physical propulsion system, shown attached to the testbed in Figure 4.2, was made up of a modified APC 12x4.5MR propeller, attached to a T-motor MT2814 770 Kv by a VPP101 Pro variable pitch linkage from Maxx Products International LLC. Power conversion for the motor was provided by a Zubax Robotics Orel 20 Electronic Speed Controller. The pitch of the propeller was actuated by a Hitec HS-5087MH servo. Actuator control, sensor measurement, control algorithm computation, and data logging

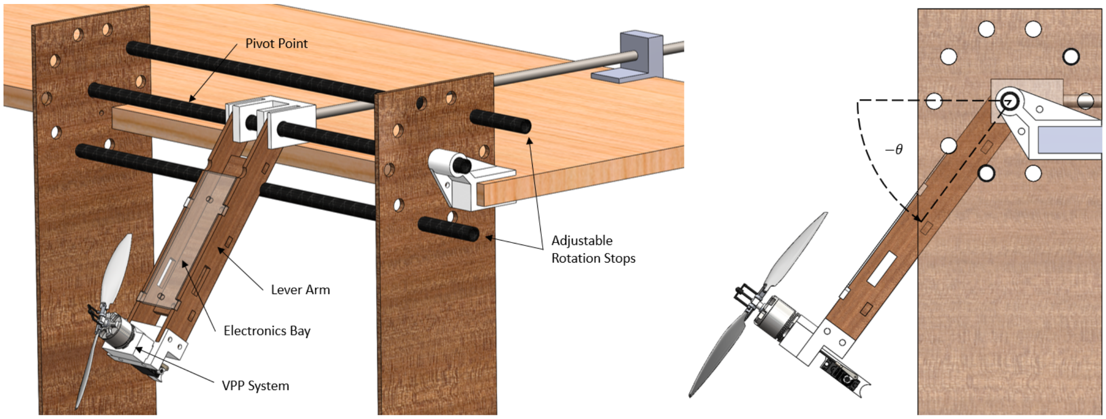

Figure 4.1: Design of the table-mounted testbed for controller validation in static thrust conditions.

were accomplished by a Pixhawk V1 flight controller. Pitch and motor speed control algorithms were implemented in the PX4 firmware stack and loaded onto the Pixhawk. Actuator commands were sent to the motor and pitch servo via CAN bus and PWM communication protocols, respectively. By mounting the Pixhawk to the testbed's Lever Arm, on-board IMU measurements of lever arm attitude were gathered.

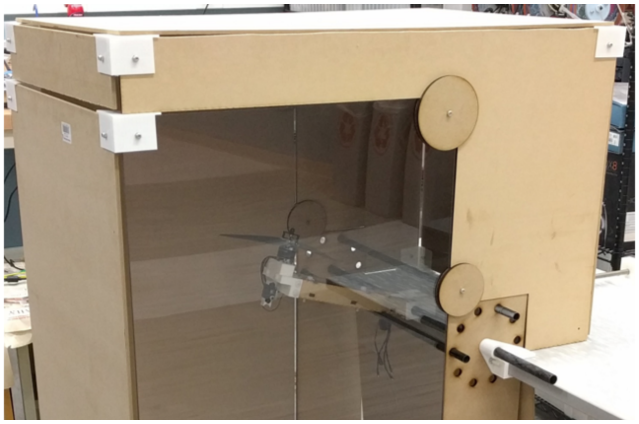

Figure 4.2: Table-mounted testbed. Structural components made from 3D-printed PLA plastic and laser-cut Medium Density Fiberboard.

4.1.2 Aerial Testbed

The experiments performed on the aerial testbed differed from the table-mounted experiments in several key ways. First, the controlled state of the aircraft was chosen to be airspeed instead of an attitude-based state; because of the nature of fixed-wing flight and the need for some constraint to be imposed on the aircraft algorithm, airspeed was the kinematic state of the glider that could be directly influenced by the propulsion system. Figure 4.1.2 shows the aerial testbed during a takeoff maneuver, during which the plane was piloted in an exclusively manual mode. Once a desired altitude range was reached, several different tests were conducted over the course of four test flights. In the first, the pitch angle of the propeller blades was kept constant in order to provide baseline performance data for comparison against controller performance. In the second, the pitch algorithm was activated and allowed to minimize power without constraint by the motor speed controller. In the third and fourth tests, both pitch and motor speed controllers were activated together, and the setpoint of the constrained state s_k^{des} was controlled by the pilot; the pilot changed the constrained state setpoint as little as possible to facilitate quasi-steady operating conditions for the controllers. In all cases, the pilot retained manual control of the rudder and elevator to steer the aircraft.


(a)

(b)

Figure 4.3: (a) The modified E-flite Radian modified with custom hardware for testing VPP performance. (b) The modified E-flite Radian during a takeoff maneuver on one of the flight tests.

All of the propulsion and avionics hardware used on the table-mounted testbed was mounted in or on the aerial testbed. In addition, sensors for gathering GPS and airspeed readings were mounted on the aerial testbed and interfaced to the Pixhawk via Serial and I2C communication protocols, respectively.

Pictured in Figure 4.4 is time-series data from both the testbed and aerial experiments, shown separately. In the testbed data in the upper frame, the noise in the arm angle and power signals comes from the motor speed controller constantly making speed adjustments in order to regulate thrust while the pitch controller decreases power consumption. Note that, in the table-top test, the speed control response time is able to regulate the arm angle to a tight tolerance because it is much faster than the response of the pitch controller. Hence, this enables power minimization to happen under well-enforced constraints. In the aerial test, the motor speed controller gains were tuned to favor stable convergence over fast convergence to a setpoint. Both controllers were active for the portion of the time-series inside the vertical, dashed lines. In spite of the relaxed convergence speed, it can be qualitatively seen that the vehicle airspeed is able to regulate airspeed fairly well until the pitch component of the glider's attitude changed suddenly at about 100 s into the flight.

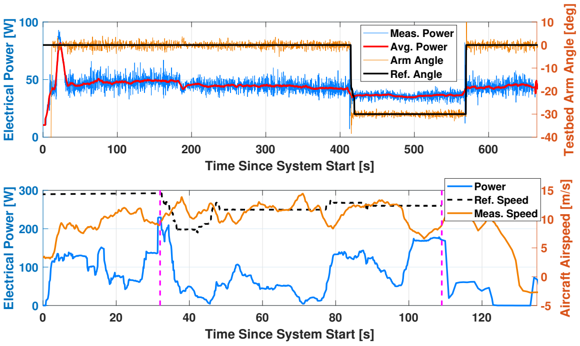

Figure 4.4: Experimental data from the testbed and aerial flight experiments, showing the electrical power consumption as well as the regulated state and state reference signal.

The data in Figure 4.5 summarizes the performance of the controllers in the two experimental contexts. Performance at the kth time step was estimated offline after the experiments as

$$\eta_k = \frac{T_k}{P_k} = \frac{C_{d,k}(V_k, \gamma_k, a_{x,k})\, V_k^2 + m_a\, g\, sin(\gamma_k) + m_a\, a_{x,k}}{P_k} \tag{4.1}$$

where T_k is the thrust produced by the VPP system, estimated from measurements of vehicle pitch γ_k, longitudinal acceleration $a_{x,k}$, and in the case of the aerial testbed, airspeed V_k and aircraft mass m_a. Electrical power consumption P_k is obtained from voltage and current measurements into the electronic speed controller. The aerial testbed drag coefficient $C_{d,k}$ was regressed from gliding data as a linear function of V_k, γ_k, and $a_{x,k}$, yielding an R-square value of 0.97. The upper frame shows that control on the testbed has marginally higher performance than baseline data from an experiment where only the thrust controller was activated across a range of manually-set pitch angles. The lower frame of Figure 4.5 shows that dual controller tends to have higher performance across the board. Linear regression of the data trends imply that the control strategy improved performance on average by 3.5% in the table-top tests and by at least 50% in the aerial tests.

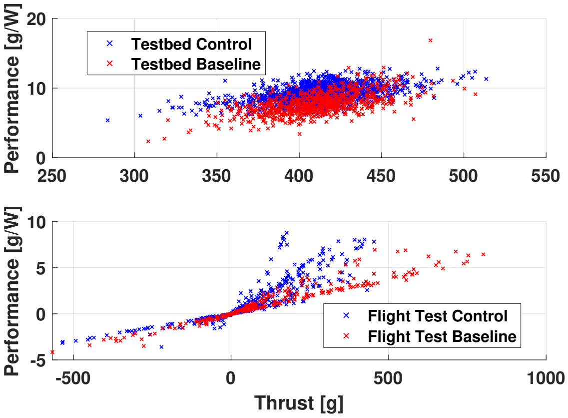

Figure 4.5: Performance summary of the data presented in Figure 4.4. Thrust is expressed in grams of mass that would produce an equivalent force under an acceleration of $9.81\,m \cdot s^{-2}$. In both experiments, the controllers produce generally higher performance, shown by the steepness of the slope in the data trend.

4.2 ES Control Validation

A number of computational validations were conducted to show the efficacy of the Extremum-Seeking control approach detailed in Section 3.2. Extensive validation of the feedforward thrust model against wind tunnel performance data of a wide array of hobby propellers was conducted to confirm the model's generality.

4.2.1 Thrust Model Validation

In order to validate the thrust model derived in Section 2.1.3, wind tunnel data from the UIUC propeller database [9] were used. For a given propeller in the database, a regression of the model coefficients was performed using thrust and air speed data, after which prediction errors for every data point were calculated; since all the propellers in this database were of constant-pitch, the pitch value in the feedforward model was set to a constant of unity. The summary regression errors with respect to propeller diameter and propeller thrust are shown in Figure 4.6. Although prediction error is present in propellers of any diameter, high prediction error is more likely to occur at thrusts below 2 N. Beyond this thrust, the prediction error rarely exceeds 20%

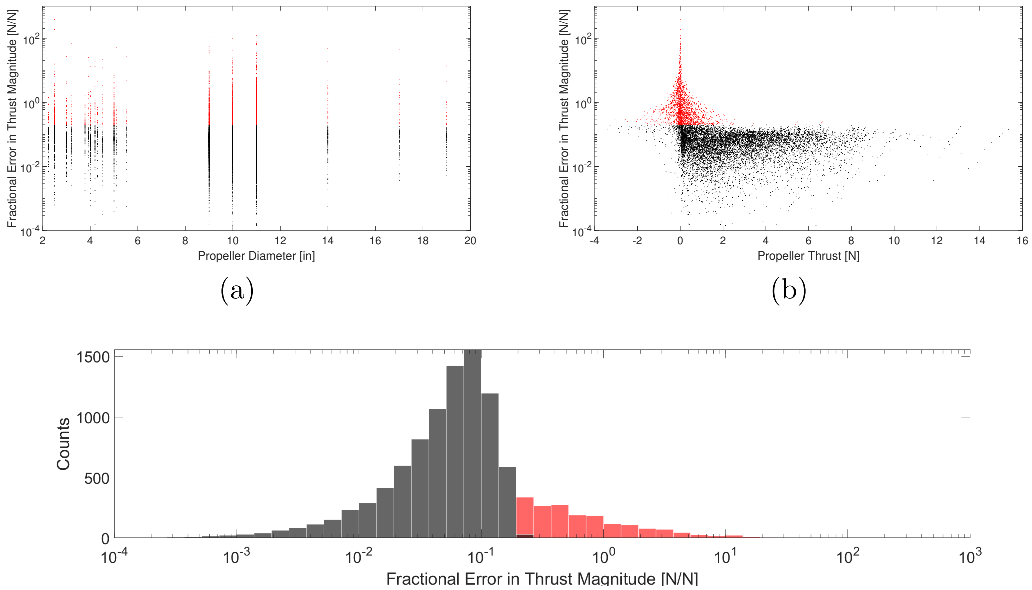

(a) (b)

(c)

Figure 4.6: Description of the magnitude of the fractional error in the prediction of wind tunnel propeller thrust using the feedforward thrust model, shown with respect to (a) propeller diameter, (b) non-normalized propeller thrust, and (c) the frequency of obtaining a certain prediction error.

A strength of this data set is that it has a wide variety of propeller sizes and designs, showing the model's flexibility in approximating different propeller designs and variations of nominal propeller pitch. However, a weakness of this wind tunnel data is that it does not explicitly have collective pitch as a variable for the propellers in the database, and therefore it does not test this parameter in the thrust model. Future testing would need to be done with a data set that has collective pitch data to produce a strong validation of the model.

4.2.2 Controller Stability

Furthermore, several simulations were conducted to test control algorithm performance under several virtual flight scenarios. A still-air environment at standard temperature and sea-level pressure was assumed, and vehicle dynamics were modeled according to Equation 2.1 with aircraft attitude θ corresponding to the level flight configuration. The dynamics of the mechanical actuators in the VPP system were modeled as first-order filters according to Equations 2.7 and 2.10. Virtual sensors in the simulated environment measured axial air velocity, motor speed, servo horn angle, electrical power consumption and axial linear acceleration. Measurements of each state were corrupted with zero-mean gaussian noise at 0.1% of the characteristic maximum value of that state. Fluid flow dynamics of the propeller were numerically calculated by Drela's QPROP solver [34]. Motor constants for a T-motor MT2814 770kv and a propeller model for an APC 10x4.7 slow flyer propeller were supplied to QPROP. The update rate of the control algorithm was run at 50 Hz for all simulated scenarios, representative of the order-of-magnitude update rate of the Pixhawk flight controller.

Stability of the thrust-tracking, power-minimizing controller is shown for two fundamental thrust reference types: constant thrust reference and a simulated reduction in thrust. The PI gains used for these simulations were drawn from Section 3.2.1 and are $K_p = 0.0398,\ K_i = 12.5$, and the value of the integration gain k in the Extremum-Seeking controller is -6. One of the advantages of the feedforward thrust model is that it allows estimation of the actuation limits on thrust with respect to motor speed and servo angle. To demonstrate this feature, motor speed was limited to 90 % of its characteristic maximum.

Figure 4.7 shows the controller's convergence to a constant thrust reference. Initially, the thrust reference takes a value of $T_{ref} = 4\ N$ when $t \in [0, 40)\ s$. From 40 s onward, the thrust reference is 8 N. The step change in the thrust reference was given to provide a look at the behavior of thrust and pitch control laws to abrupt change in setpoint. The

EKF initially takes about 200 samples to stabilize the thrust feed-forward model. The thrust converges to within 0.1 N in about 2.25 s. The thrust model converges to within 0.1 N in almost 10 s. The servo horn pitch angle, seen in the upper right-hand panel, is set to an initial condition of 15°. Integration of the best-estimate servo angle $\hat{\zeta}$ is speed-limited to half of the max perturbation speed until the thrust controller is allowed to reach an approximately steady state. Once the approximately steady-state condition is met, the limit on integration speed is increased to 4 times the max perturbation speed. This change in integration speed limit happens about 8 s into the simulation.

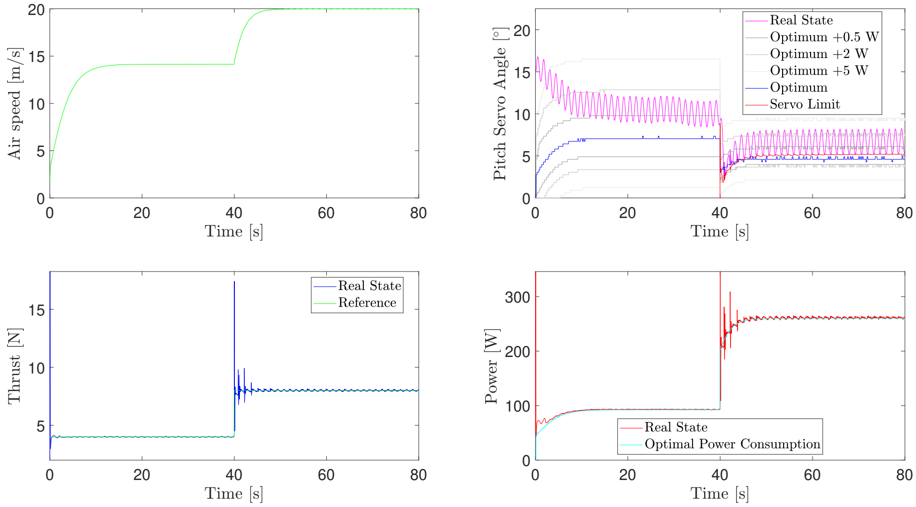

Figure 4.7: Convergence of controller to a constant reference followed by a step increase. An integrator constant of $k = -6$ was used.

From this point on, the convergence rate makes only slight progress toward the optimal configuration; the most probable reason for this is that the EKF seems to be continually refining the feed-forward to thrust model. A second reason for the seeming loss in intentional convergence is due to the presence of noise in the measurements. For instance, the 0.1% variance on the measurement of power consumption is relative to a 500 W characteristic maximum value, translating to a standard deviation of $\sigma = 0.7\ W$. This is approximately the same order of magnitude as the error in the estimate of the steady-state optimum.

Figure 4.8 shows more clearly that the feed-forward model learning is effective under a variable reference scenario of sufficiently low frequency. As the thrust setpoint increases, the estimated lower bound on servo angle forces ζ away from the minimum-power region. Although this has a high power cost, the benefit is that the thrust setpoint is maintained. From the time that the servo angle disengages from the lower bound, the time taken to enter the $(P_{opt} + 5)\ W$ region is approximately 6 s.

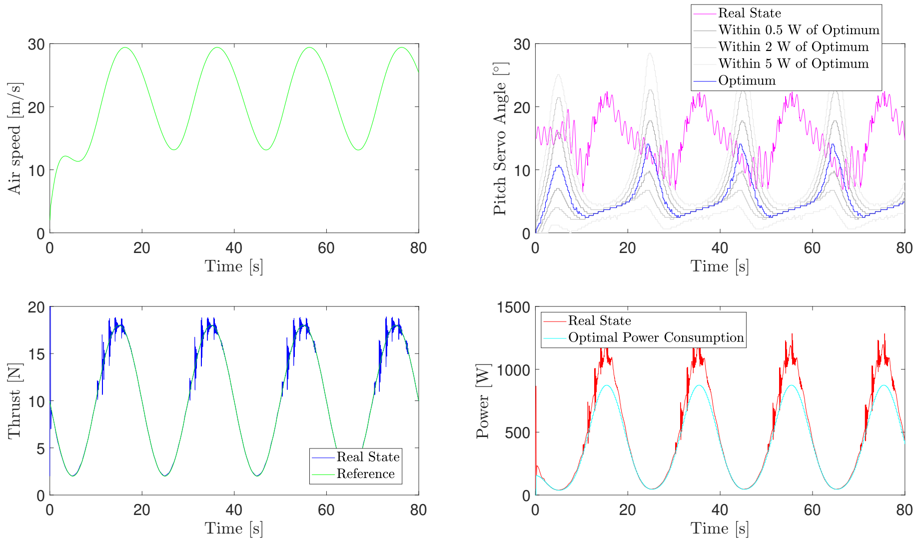

Figure 4.8: Behavior of the Extremum Seeking algorithm under a sinusoidal load with upper limit on motor speed.

The previous simulation took actuation limits into account. Figure 4.9 shows the behavior of the ES algorithm with no simulated limit on reachable speed. The algorithm is able to repeatably bring the servo angle to a near-optimum configuration even in the face of the low-frequency fluctuations caused by the oscillating thrust reference. The importance of the feed-forward model is seen by comparing the tracking of the optimum servo angle during the first period of high thrust with the tracking one period later in the thrust reference sine wave. Furthermore, under this scenario and current ES algorithm tuning, the system is restored to operating within approximately 5 W of optimum about 5 s after exceeding the 5 W envelope.

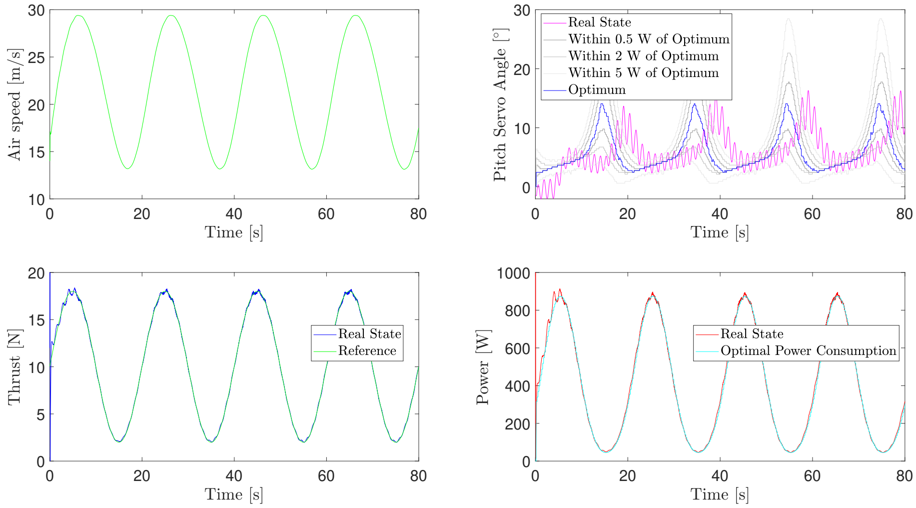

Figure 4.9: Convergence of the real thrust and thrust feed-forward model to a sinusoidal-constant reference with $k = -6$.

4.2.3 Performance

To get a figure of the control algorithm's ability to minimize power consumption, the total amount of energy consumed during the aforementioned tests was measured and compared with energy use under optimal servo angle control. The results are displayed in Table 4.1.

Algorithm	**Constant Thrust**	**Sinusoidal Thrust**	**Units**
Best Constant Pitch	92	509	W
Algorithm	93(+7)	418(+7)	W
Algorithm (limits)	93(+7)	474(+7)	W
Optimal Pitch	92	407	W

Table 4.1: Average power consumption for each simulation scenario under the investigated control policies.

Performance of power minimization is calculated against a numerically-calculated optimal servo angle at the current air speed and thrust. The servo angle is moving toward the steady-state optimal value at a rate of approximately 0.1 $[deg/s]$ in Figure 4.7, although the rate does slow down as it approaches the optimal point. Part of this is due to the fact that the energy well has very shallow concavity. In Figure 4.9, the servo angle is decreasing, though at a very slow rate. Tuning the extremum seeking controller will be a subject of future work.

4.3 Summary

The computational and experimental validations shown in this chapter document the development of an algorithm for controlling the thrust of a Variable-Pitch Propulsion System while minimizing power cost. Although the physical testbeds demonstrated that this objective was possible with the simple control laws of PID and P&O, the susceptibility to disturbances showed the need for the improved control algorithm of Section 3.2.

Wind tunnel data was used to test feedforward thrust model validity. The improved controller was tested in several simulation scenarios. Performance of the improved control framework showed adequate thrust tracking during power optimization and significant power reduction compared to best-case constant-pitch propeller even assuming a worst-case power cost from the pitch servo.

Chapter 5

Conclusion and Future Work

This paper presents a study of control frameworks for a variable-pitch propulsion system for efficiently propelling VTOL UAVs. A simple controller using a PID law and a Perturb Observe algorithm was implemented on a forward-flying UAV to observe the algorithm performance in a physical system. Improvements were made to the algorithm were made by replacing or supplementing portions of the control framework. The linear feedback thrust controller was designed to be robust to considerable variations in plant parameters. This feedback signal was summed with an adaptive nonlinear feedforward thrust model. An Extended Kalman Filter provided the mechanism for learning the thrust model parameters, thereby enabling better thrust tracking performance as well as the observation of thrust reachability limits. More stable power minimization was achieved by replacing the Perturb Observe pitch servo control algorithm with an Extremum-Seeking adaptive control scheme. Several safety mechanisms were put in place to ensure that the power optimization process is not deleterious to thrust tracking performance.

Several simulation studies were performed to show the safety and stability of the control framework under several characteristic inputs. Time-domain performance metrics showed the convergence of the motor speed controller in fractions of a second and the thrust model convergence within about 10 seconds. Convergence of the servo angle to a near-optimal behavior was on the order of 6 seconds, with refinements occurring up to 60 seconds from initialization.

Future research avenues that would be valuable to explore include the incorporation of vehicle drag into the learning model for thrust so that the controller could based around air speed setpoints. Implementing a cumulative learning element into the pitch control algorithm would improve convergence speed to optimal configuration and allow the perturbation of the Extremum-Seeking control to be employed only when new portions of the power manifold are being explored. Additionally, the components of the algorithm should be validated with physical experiments to test the generality of the thrust model, the stability of the Extremum-Seeking process under thrust regulation, and the robustness of the linear feedback motor speed controller during VTOL flight maneuvers.

Efficient propulsion for VTOL aircraft extends flight time and enlarges the flight envelope, thereby increasing aerial sensing aircraft utility. If properly controlled, the Variable Pitch Propulsion system has the potential to significantly boost system efficiency across the board. This thesis focuses on some of the main control questions for applying Variable Pitch Propulsion to efficient VTOL aircraft, and though there is much left to be studied about this problem, it is the authors expectation that interest in this problem will persevere as requirements on UAVs become more extreme.

References

[1] B. Brandt, John and Michael Selig. Propeller Performance Data at Low Reynolds Numbers. In *49th AIAA aerospace sciences meeting*, volume 20, pages 2011–1255, July 2011.

[2] M. Dunbabin and L. Marques. Robots for Environmental Monitoring: Significant Advancements and Applications. *IEEE Robotics Automation Magazine*, 19(1):24–39, March 2012.

[3] W. Immerzeel, P. Kraaijenbrink, J. Shea, A. Shrestha, F. Pellicciotti, M. Bierkens, and S. de Jong. High-Resolution Monitoring of Himalayan Glacier Dynamics Using Unmanned Aerial Vehicles. *Remote Sensing of Environment*, 150:93 – 103, 2014.

[4] E. Honkavaara, H. Saari, J. Kaivosoja, I. Pölönen, T. Hakala, P. Litkey, J. Mäkynen, and L. Pesonen. Processing and Assessment of Spectrometric, Stereoscopic Imagery Collected Using a Lightweight UAV Spectral Camera for Precision Agriculture. *Remote Sensing*, 5(10):5006–5039, 2013.

[5] N. Metni and T. Hamel. A UAV for Bridge Inspection: Visual Servoing Control Law with Orientation Limits. *Automation in Construction*, 17(1):3–10, 2007.

[6] Z. Li, Y. Liu, R. Hayward, J. Zhang, and J. Cai. Knowledge-Based Power Line Detection For UAV Surveillance and Inspection Systems. In *23rd International Conference on Image and Vision Computing.*

[7] S. Hrabar I. Sa and P. Corke. Inspection of Pole-Like Structures Using a Vision-Controlled VTOL UAV and Shared Autonomy. In *International Conference on Intelligent Robots and Systems*, pages 1–6, November 2014.

[8] S. Siebert and J. Teizer. Mobile 3D Mapping for Surveying Earthwork Projects Using an Unmanned Aerial Vehicle (UAV) System. *Automation in Construction*, 41:1 – 14, 2014.

[9] J. Brandt, R. Deters, G. Ananda, and M. Selig. UIUC Propeller Database. `http://m-selig.ae.illinois.edu/props/propDB.html`.

[10] C. Poulson. Airscrew-Engine Combinations and Their Effect on The Take-off. *Flight International Magazine*, 1935.

[11] K. C. Wong, J. A. Guerrero, D. Lara, and R. Lozano. Attitude Stabilization in Hover Flight of a Mini Tail-Sitter UAV with Variable Pitch Propeller. In *2007 International Conference on Intelligent Robots and Systems*, pages 2642–2647, October 2007.

[12] M. Cutler and J. P. How. Analysis and Control of a Variable-Pitch Quadrotor for Agile Flight. *Journal of Dynamic Systems, Measurement, and Control*, 137(10), 2015.

[13] K. Kawasaki, M. Zhao, K. Okada, and M. Inaba. MUWA: Multi-Field Universal Wheel for Air-Land Vehicle with Quad Variable-Pitch Propellers. In *2013 IEEE/RSJ International Conference on Intelligent Robots and Systems*, pages 1880–1885, Nov 2013.

[14] N. Gupta, M. Kothari, and A. Abhishek. Flight Dynamics and Nonlinear Control Design for Variable-Pitch Quadrotors. In *2016 American Control Conference*, pages 3150–3155, July 2016.

[15] P. Panizza, D. Invernizzi, F. Riccardi, S. Formentin, and M. Lovera. Data-Driven Attitude Control Law Design for a Variable-Pitch Quadrotor. In *2016 American Control Conference*, pages 4434–4439, July 2016.

[16] M. Cutler, N. M. Ure, B. Michini, and J. P. How. Comparison of Fixed and Variable Pitch Actuators for Agile Quadrotors. In *2011 AIAA Guidance, Navigation, and Control Conference*, pages 1–17, August 2011.

[17] T. Cazenave, M. Pakmehr, and E. Feron. Peak-Seeking Control of a DC Motor Driving a Variable Pitch Propeller. In *2011 AIAA Guidance, Navigation, and Control Conference*, pages 1–10, August 2011.

[18] E. Fresk and G. Nikolakopoulos. Experimental Model Derivation and Control of a Variable Pitch Propeller Equipped Quadrotor. In *2014 IEEE Conference on Control Applications*, pages 723–729, October 2014.

[19] S. Sheng and C. Sun. Control and Optimization of a Variable-Pitch Quadrotor with Minimum Power Consumption. *Energies*, 9(4), 2016.

[20] R. D'Sa, D. Jenson, T. Henderson, J. Kilian, B. Schulz, M. Calvert, T. Heller, and N. Papanikolopoulos. SUAV:Q - An Improved Design for a Transformable Solar-Powered UAV. *IEEE/RSJ International Conference on Intelligent Robots and Systems (IROS)*, October 2016.

[21] R. D'Sa, T. Henderson, D. Jenson, M. Calvert, T. Heller, B. Schulz, J. Kilian, and N. Papanikolopoulos. Design and Experiments for a Transformable Solar-UAV. *IEEE International Conference on Robotics and Automation (ICRA)*, May 2017.

[22] D. Jenson, R. D'Sa, T. Henderson, J. Kilian, B. Schulz, and N. Papanikolopoulos. Energy Characterization of a Transformable Solar Powered UAV. *IEEE/RSJ International Conference on Intelligent Robots and Systems (IROS)*, October 2017.

[23] T. Henderson and N. Papanikolopoulos. Power-Minimizing Control of a Variable Pitch Propulsion System for Versatile Unmanned Aerial Vehicles. In *2019 IEEE Conference on Robotics and Automation*, May 2019.

[24] T. Henderson and N. Papanikolopoulos. Adaptive Control of Variable-Pitch Propellers: Pursuing Minimum-Effort Operation. In *2020 IEEE International Conference on Robotics and Automation*, May-June 2020.

[25] R. Gill and R. D'Andrea. Propeller Thrust and Drag in Forward Flight. In *2017 IEEE Conference on Control Technology and Applications (CCTA)*, pages 73–79, Aug 2017.

[26] N. Femia, G. Petrone, G. Spagnuolo, and M. Vitelli. Optimization of perturb and observe maximum power point tracking method. In *IEEE Transactions on Power Electronics*, volume 20, pages 963–973, July 2005.

[27] M. Krstic. *SISO Scheme and Linear Analysis*, chapter 1, pages 1–20. John Wiley Sons, Ltd, 2004.

[28] M. Krstic, A. Ghaffari, and S. Seshagiri. Extremum Seeking for Wind and Solar Energy Applications. In *Proceeding of the 11th World Congress on Intelligent Control and Automation*, pages 6184–6193, June 2014.

[29] P. Carpenter and B. Fridovich. Effect of a Rapid Blade-Pitch Increase on the Thrust and Induced-Velocity Response of a Full-Scale Helicopter Rotor. *National Advisory Committee For Aeronautics*, November 1953.

[30] J. Eldredge and C. Wang. High-Fidelity Simulations and Low-Order Modeling of a Rapidly Pitching Plate. *40th Fluid Dynamics Conference and Exhibit.*

[31] D. Raviv and E. W. Djaja. Technique for Enhancing the Performance of Discretized Controllers. *IEEE Control Systems Magazine*, 19(3):52–57, June 1999.

[32] S. Skogestad and I. Postlethwaite. *Multivariable Feedback Control: Analysis and Design.* John Wiley Sons, Ltd, The Atrium, Southern Gate, Chichester, West Sussex PO19 8SQ, England, 2010.

[33] A. Tagliabue, X. Wu, and M. W. Mueller. Model-free online motion adaptation for optimal range and endurance of multicopters. In *2019 International Conference on Robotics and Automation (ICRA)*, pages 5650–5656, May 2019.

[34] M. Drela. QPROP Formulation. `http://web.mit.edu/drela/Public/web/qprop/qprop_theory.pdf`, 2006.

Appendix A

Glossary and Acronyms

Care has been taken in this thesis to use jargon only when necessary or efficient. It was deemed necessary to clarify a few terms more precisely for the reader, which are listed below.

A.1 Glossary

- **Fixed-wing** (**FW**) – An aircraft with a geometric and functional typology such that its characteristic flight mode is in a persistent horizontal direction. Such aircraft usually exhibit one or more wings for producing vertical lift.
- **Multi-rotor** (**MR**) – An aircraft with a geometric and functional typology such that its characteristic flight mode is a hovering or vertical movement direction. Such aircraft usually exhibit one or more thrust-producing actuators which provide vertical lift.

A.2 Acronyms

Table A.1: Acronyms

Acronym	Meaning
UAV	Unmanned Aerial Vehicle
VPP	Variable Pitch Propulsion
ES	Extremum Seeking
P&O	Perturb and Observe
PID	Proportional-Integral-Derivative (Control)
KF / EKF	Kalman Filter / Extended Kalman Filter
COTS	Commercial Off-The-Shelf
BET / BEMT	Blade Element Theory / Blade Element Momentum Theory
CFD	Computational Fluid Dynamics
AoA / α	Angle of Attack
VTOL	Vertical Takeoff and Landing
PPT / MPPT	(Maximum) Power Point Tracker/ing